



Conjugated polyene-modified Bi_2MO_6 ($\text{M}=\text{Mo}$ or W) for enhancing visible light photocatalytic activity



Haiping Li^a, Wanguo Hou^{b,*}, Xutang Tao^c, Na Du^b

^a National Engineering Technology Research Center for Colloidal Materials, Shandong University, Jinan 250100, PR China

^b Key Laboratory of Colloid and Interface Chemistry (Ministry of Education), Shandong University, Jinan 250100, PR China

^c State Key Laboratory of Crystal Materials, Shandong University, Jinan 250100, PR China

ARTICLE INFO

Article history:

Received 11 December 2014

Received in revised form 3 February 2015

Accepted 8 February 2015

Available online 10 February 2015

Keywords:

Polyene

Electron reservoir

Photocatalytic

Bi_2MO_6

Bi_2WO_6

ABSTRACT

Nanohybrids of Bi_2MO_6 ($\text{M}=\text{Mo}$ or W) and a conjugated polyene (CP) were successfully prepared by calcining precursor Bi_2MO_6 /polyvinyl alcohol composites. The morphology, structure, and photocatalytic performance of the nanohybrids were investigated. The CP adheres to the surface of the Bi_2MO_6 hollow microspheres via the metal (Bi and Mo or W)—O—C bonds. Coordination interactions between the hydroxyl groups in polyvinyl alcohol and the metal (Bi and Mo or W) atoms in Bi_2MO_6 promote the formation of metal—O—C bonds in the calcination process. For the degradation of the model pollutant, Rhodamine B (RhB), under visible light irradiation, the Bi_2MO_6 /CP and Bi_2WO_6 /CP nanohybrids exhibit photocatalytic efficiencies that are, respectively, four times and twice those of the corresponding pure Bi_2MO_6 . The photocatalytic activity enhancement stems from the electron transfer through the metal—O—C bonds between Bi_2MO_6 and CP. Interestingly, two different mechanisms by which CP enhances the photocatalytic activity of Bi_2MO_6 were confirmed. For the Bi_2MO_6 /CP nanohybrids, the CP acts as an electron reservoir, accepting and shuttling the electrons from Bi_2MO_6 . For the Bi_2WO_6 /CP nanohybrids, however, the CP acts as a photosensitizer, injecting electrons into Bi_2WO_6 . The nanohybrids both exhibit good recyclability. The photocatalytic performance of the Bi_2MO_6 /CP nanohybrids is comparable with that reported for Bi_2MO_6 modified using expensive conjugated carbon materials (CCMs) such as graphenes, fullerenes (e.g., C_{60}), and carbon nanotubes. Thus, CP is an ideal substitute for these expensive CCMs in the preparation of composite photocatalysts, because of its low cost and simple preparation process.

© 2015 Elsevier B.V. All rights reserved.

1. Introduction

Semiconductor photocatalysis is considered to be a promising and environmentally friendly technology for solving the global energy and environment crises, because it can harvest sunlight as an energy source to produce hydrogen by splitting water [1], reduce carbon dioxide to form hydrocarbon fuels [2], and degrade harmful environmental pollutants [3]. Several types of photocatalysts have been developed, such as semiconductors based on Ti [4], Zn [5], Bi [3,6], Ag [7], and Cu [8], as well as CdS [9] and graphitic carbon nitride [10,11]. Among these, however, only TiO_2 and nitrogen doped TiO_2 (N- TiO_2) have been applied on a small industrial scale in self-cleaning glass and indoor air purification [12,13]. Photocatalysts have not been used on a large scale for water splitting and degradation of industrial pollutants because of their low photocat-

alytic efficiencies. Therefore, catalytic scientists are now focusing on enhancing the photocatalytic efficiency of photocatalysts.

Many factors influence the activity of photocatalysts, such as the particle size [14], specific surface area [15], and band gap [16], as well as the morphology and structure of the surface [17,18]. The surface structure of photocatalysts is a key factor because photocatalytic reactions are caused by photoinduced electrons and holes on the surface [17,18]. Nanohybrid (composite) or heterojunction construction is one of the most studied ways to modify the surface structures and enhance the photocatalytic efficiency of photocatalysts [3]. Tremendous interest in the use of conjugated carbon materials (CCMs), such as graphenes, carbon nanotubes (CNTs), and fullerenes (e.g., C_{60}), to modify semiconductors has been triggered by their high electron mobilities, high specific surface areas, wide absorption wavelength ranges, chemical inertness, and thermal stabilities [19]. Thousands of CCM-containing photocatalysts have been developed [20,21]. Two mechanisms were proposed for the photocatalytic activity enhancement of photocatalysts induced by the CCMs. In the first mechanism, the CCMs act as photosensitizers

* Corresponding author. Tel.: +86 531 88365460; fax: +86 531 88364750.
E-mail address: wghou@sdu.edu.cn (W. Hou).

to extend the optical absorption ranges of photocatalysts, providing additional electrons to the conduction band (CB) of semiconductors [19,22–24]. In the second mechanism, the CCMs act as electron reservoirs, reducing electron-hole recombination, prolonging the lifetime of the charge carriers, and improving the quantum yield [7,22–24].

Much fundamental research has been done on CCM-modified semiconductor photocatalysts in recent years [19–21], but there is still a lot of work to do before they can be used industrially because of the complicated preparation process and high cost of these CCMs. Thus, it is necessary to seek inexpensive substitutes for graphenes, CNTs, and C_{60} to make the technology economically feasible. More recently, Lei et al. [25] found that the conjugated polyene (CP) which is formed via dehydration of polyvinyl alcohol (PVA) by calcination could greatly enhance the photocatalytic efficiency of TiO_2 by acting as a photosensitizer. This CCM is simple and inexpensive to prepare, indicating a good prospect for industrial application as a substitute for graphenes, CNTs, and C_{60} .

Bi_2MoO_6 and Bi_2WO_6 , denoted as Bi_2MO_6 ($M=Mo$ or W), are the simplest members of the layered Aurivillius-related oxide family, and consist of $[Bi_2O_2]^{2+}$ layers sandwiched between MO_4^{2-} slabs. As Bi-based ternary metal oxide photocatalysts, they usually exhibit excellent photocatalytic activity under visible light irradiation [3,26,27]. Heterojunction construction is capable of enhancing the photocatalytic performance of Bi_2MO_6 . We have built $Bi_2MoO_6/Zn-Al$ layered double hydroxide and $Bi_2MoO_6/g-C_3N_4$ heterojunctions [28,29] to increase the photocatalytic activity of the catalysts. Notably, Bi_2MO_6 modified with graphene or C_{60} exhibited significantly increased photocatalytic efficiency [30–34]. It would be interesting if CP could replace graphene and C_{60} to enhance the photocatalytic performance of Bi_2MO_6 .

In this study, nanohybrids of CP-modified Bi_2MO_6 hierarchical hollow microspheres were prepared by a simple calcination method. The photocatalytic efficiency of the nanohybrids for degrading the model pollutant Rhodamine B (RhB) was investigated under visible light irradiation. As expected, our data indicated that the modification of Bi_2MO_6 with CP can obviously enhance its photocatalytic efficiency, which is comparable with the results with graphene or C_{60} modification. Interestingly, different functions of CP were found in the Bi_2MoO_6/CP and Bi_2WO_6/CP systems. For the Bi_2MoO_6/CP nanohybrids, CP acted as an electron reservoir, while for the Bi_2WO_6/CP nanohybrids, it acted as a photosensitizer. It is easy to obtain CP by calcining inexpensive polymers such as PVA and polyvinyl chloride. This study reveals that this inexpensive CP is a promising substitute for graphene, C_{60} , and CNTs when modifying semiconductors to enhance their photocatalytic performance.

2. Experimental

2.1. Materials

Ethanol, ethylene glycol, RhB, methyl violet 2B, sodium tungstate ($Na_2WO_4 \cdot 2H_2O$), sodium molybdate ($Na_2MoO_4 \cdot 2H_2O$), and bismuth nitrate ($Bi(NO_3)_3 \cdot 5H_2O$) were purchased from Aladdin (China). PVA with an average polymerization degree of 1700 and alcoholysis degree of 98–99% was purchased from Shanghai Titanchem Co., Ltd. (China). Commercial N- TiO_2 with a N content of about 4% was purchased from Xuan Cheng Jing Rui New Material Co., Ltd. (China). All the chemicals were used as received. Water was obtained from a Hitech-Kflow water purification system (Hitech, China).

2.2. Preparation of Bi_2MO_6/CP nanohybrids

Bi_2MO_6 ($M=Mo$ or W) substrates used in this study were synthesized according to the literature [27] (S1, Supporting information).

The Bi_2MO_6/CP nanohybrids were synthesized by the calcination method described by Lei et al. [25] 1.0 g of Bi_2MO_6 powders was dispersed in 20 ml of H_2O by ultrasonication for 20 min. A calculated amount of PVA solution (50 g/L) was then added to the suspension. The mass ratio of PVA to Bi_2MO_6 in the system was 1, 2, or 5 wt%, and that of PVA to Bi_2WO_6 was 1, 2, or 4 wt%. After stirring vigorously for 30 min, 100 ml of ethanol was slowly added dropwise into the dispersion to precipitate the PVA. The resultant composite precursor was collected by filtration, washed with ethanol, and dried at 60 °C. The nanohybrid product was obtained by calcining the precursor at 225 ± 5 °C for 2 h. The Bi_2MoO_6/CP samples obtained with PVA/ Bi_2MoO_6 mass ratios of 1, 2, and 5 wt% were denoted as MP-1, MP-2, and MP-5, and the Bi_2WO_6/CP samples obtained with PVA/ Bi_2WO_6 mass ratios of 1, 2, and 4 wt% were denoted as WP-1, WP-2, and WP-4, respectively. The theoretical contents (as mass percentages) of CP in MP-1, MP-2, and MP-5 are 0.6, 1.2, and 2.9 wt%, and those in WP-1, WP-2, and WP-4 are 0.6, 1.2, and 2.3 wt%, respectively.

For comparison, CP was prepared by calcining PVA at 225 ± 5 °C for 2 h. Mechanical mixtures of Bi_2MoO_6/CP (MP-mix) and Bi_2WO_6/CP (WP-mix) with a CP content of ~1.6% were prepared by grinding their mixtures for 5 min (S2, Supporting information).

2.3. Characterization

Powder X-ray diffraction (XRD) was carried out using a D8 ADVANCE diffractometer (Bruker, Germany), with Cu K α radiation ($\lambda = 1.54184$ Å). Attenuated total reflectance/Fourier-transform infrared (FT-IR) spectra were recorded on a Nicolet iS5 spectrophotometer (ThermoFisher, USA). UV–vis diffuse reflectance spectra were obtained on a U-4100 spectrophotometer (Hitachi, Japan), with a $BaSO_4$ reference. Thermogravimetric (TG) and differential scanning calorimetric (DSC) analyses were carried out on a SDT Q600 thermal analyzer (TA Instruments, USA), by heating from 25 to 800 °C, at a rate of 10 °C/min in air. X-ray photoelectron spectroscopy (XPS) was performed on a Thermo Scientific Escalab 250Xi spectrometer (UK) with Al K α radiation. Solid-state ^{13}C NMR spectra were recorded on an Avance III 600 (600 MHz) spectrometer (Bruker, Germany). Morphologies were examined with a Supra55 field emission-scanning electron microscope (SEM) (Zeiss, USA), a JEM-1011 transmission electron microscope (TEM, Jeol, Japan) and a JEM-2100F high-resolution TEM (HRTEM, Jeol, Japan). The spatial elemental distribution of nanohybrids was investigated by EDS and elemental mapping analysis, using the SEM instrument equipped with an energy dispersive X-ray spectrometer. Selected area electron diffraction (SAED) patterns were obtained using the HRTEM. Photoluminescence (PL) spectra were measured using an F-7000 spectrophotometer (HITACHI, Japan) with an excitation wavelength of 400 nm. The excitation and emission slit widths were set at 10 nm. Time-resolved fluorescence was measured using an Edinburgh Analytical Instruments FLS920 time-resolved spectrofluorometer (UK), using the time-correlated single photon counting method, with an excitation wavelength of 370 nm. Specific surface areas were probed by measuring volumetric N_2 adsorption–desorption isotherms at liquid nitrogen temperature, using a Tristar II 3020 instrument (Micromeritics, USA). Samples were degassed at 150 °C for 3 h under vacuum before measurements.

2.4. Photocatalytic activity measurement

The photocatalytic performance of the as-prepared photocatalysts was evaluated by degrading the model pollutant RhB at room temperature using a XPA-7 photocatalytic reaction equipment (Xujiang Electromechanical Plant, China) [28]. A 400 W metal halide lamp equipped with an ultraviolet cutoff filter ($\lambda \geq 420$ nm)

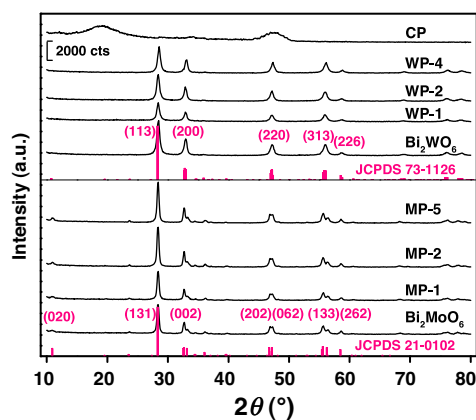


Fig. 1. XRD patterns of Bi_2MO_6 , CP and their nanohybrids.

and a 500 W mercury lamp equipped with a visible cutoff filter ($\lambda \leq 365$ nm) were used as the visible and ultraviolet light sources, respectively. For each run, 0.05 g of photocatalyst was added to 50 mL of RhB (10 mg/L) solution. Prior to irradiation, the suspension was stirred in the dark for 1 h to ensure sorption equilibrium. After a given irradiation time, ~4 mL aliquots of dye solutions were collected. These were centrifuged ($10,300 \times g$) for 10 min and analyzed using a Hewlett-Packard 8453 UV–vis spectrophotometer (USA) at a wavelength of 554 nm. The ratio of remaining dye concentration to its initial concentration, C/C_0 , was obtained by calculating the ratio of the corresponding absorbance. Recycling reactions [29] were carried out to evaluate the stability of the $\text{Bi}_2\text{MO}_6/\text{CP}$ nanohybrids.

3. Results and discussion

3.1. Characterization of $\text{Bi}_2\text{MO}_6/\text{CP}$ nanohybrids

The morphologies and structures of the precursors have a large effect on the features of the final products [35]. The SEM and TEM images of Bi_2MO_6 samples synthesized by a hydrothermal method [27] show hierarchical hollow microspheres with diameters from hundreds of nanometers to several micrometers (Fig. S1, Supporting information).

The XRD patterns of the Bi_2MO_6 samples exhibit their characteristic diffractions (Fig. 1). For Bi_2MoO_6 , the peaks at 28.4 , 32.7 , 46.9 , and 55.6° are indexed to the (1 3 1), (0 0 2), (0 6 2), and (1 3 3) planes of orthorhombic Bi_2MoO_6 (JCPDS file 21-0102), respectively. For Bi_2WO_6 , the peaks at 28.5 , 32.9 , 47.2 and 55.9° correspond to the (1 3 3), (2 0 0), (2 2 0), and (3 1 3) planes of orthorhombic Bi_2WO_6 (JCPDS file 73-1126), respectively. No peaks indicating impurities are observed, demonstrating that the Bi_2MO_6 samples have good crystallinity and purity.

PVA is prone to adhere to the surface of the metal oxides after precipitation from the suspensions [25]. Interactions between PVA and Bi_2MO_6 were identified using FT-IR, TG, and DSC analyses (Figs. S2 and S3, Supporting information). The FT-IR spectra of the $\text{Bi}_2\text{MO}_6/\text{PVA}$ precursors present the characteristic absorption bands of PVA [36,37] and Bi_2MO_6 [38,39]. The formation of a composite of PVA and Bi_2MO_6 induces the blue shifts of the O–H stretching band of PVA, from 3295 to 3368 cm^{-1} for $\text{Bi}_2\text{MoO}_6/\text{PVA}$ and to 3422 cm^{-1} for $\text{Bi}_2\text{WO}_6/\text{PVA}$, while it induces the redshifts of the Mo–O stretching band of Bi_2MoO_6 (from 713 to 708 cm^{-1}) and the W–O stretching band of Bi_2WO_6 (from 708 to 696 cm^{-1}) (Fig. S2). These absorption peak shifts indicate that coordination between the OH groups in PVA and the metal (Bi and Mo or W) atoms in Bi_2MO_6 occurs in the precursors [37,40]. The coordination interactions are favorable for the formation of metal –O–C bonds

in the calcination process. The TG and DSC results also demonstrate the presence of PVA– Bi_2MO_6 interactions (Fig. S3). Pure PVA is completely decomposed at a temperature (T) of $\sim 540^\circ\text{C}$, but T for the complete decomposition of PVA in $\text{Bi}_2\text{MO}_6/\text{PVA}$ precursors decreases to be ~ 400 – 410°C . The dehydration of PVA to form CP in the $\text{Bi}_2\text{MO}_6/\text{PVA}$ precursors occurred at $T = \sim 175$ – 260°C , while that in pure PVA occurred at $T = \sim 230$ – 390°C [40]. These results indicate that the presence of Bi_2MO_6 decreased the thermal stability of the PVA, which is attributed to the coordination interactions between Bi_2MO_6 and PVA. Thus, the calcination at $225 \pm 5^\circ\text{C}$ used for the preparation of $\text{Bi}_2\text{MO}_6/\text{CP}$ nanohybrids in this work can induce the formation of CP. According to the TG data, the CP contents in the $\text{Bi}_2\text{MO}_6/\text{CP}$ nanohybrids MP-1, MP-2, and MP-5 are evaluated to be ~ 0.8 , 1.7 , and 2.6 wt\% , and those in the WP-1, WP-2, and WP-4 are evaluated to be ~ 0.8 , 1.6 , and 2.8 wt\% , respectively. These experimental values for CP content are close to the theoretical values.

The XRD patterns of the $\text{Bi}_2\text{MO}_6/\text{CP}$ hybrids are similar to those of pure Bi_2MO_6 (Fig. 1), demonstrating that the crystal structures of Bi_2MO_6 remained unchanged after calcination. For CP, the wide diffraction peaks at 19.0 and 47.6° stem from the crystallinity of the PVA [41]. They cannot be observed in the XRD patterns of $\text{Bi}_2\text{MO}_6/\text{CP}$ hybrids due to their low CP contents.

The SEM and TEM images of $\text{Bi}_2\text{MO}_6/\text{CP}$ nanohybrids show hierarchical hollow microspheres (Fig. 2a, b, g and h), similar to those of Bi_2MO_6 (Fig. S1). That is, the hierarchical hollow microsphere morphology of Bi_2MO_6 remained stable during the calcination process. Closer examination reveals that the hierarchical hollow microspheres are composed of irregular nanosheets (Fig. 2d and j). The selected area electron diffraction (SAED) images (Fig. 2f and l) of MP-2 and WP-2 microspheres show several diffraction dots, indicating that the nanosheets are single crystals. The energy dispersive spectrometry (EDS) images show the existence of a large amount of carbon, and the elemental mapping images show the homogeneous distribution of the carbon on the surfaces of Bi_2MO_6 microspheres (Fig. 2c and i). The carbon belongs to the CP, indicating the uniform distribution of CP on the microsphere surfaces. High-resolution TEM (HRTEM) images (Fig. 2e and k) show that the CP particles adhere to the surfaces of the single crystal nanosheets of Bi_2MO_6 . The lattice fringe spacings of 0.314 and 0.250 nm correspond to the (1 3 1) plane of Bi_2MoO_6 (Fig. 2e) and the (1 1 5) plane of Bi_2WO_6 (Fig. 2k), respectively. These results indicate that the CP directly anchored on the Bi_2MO_6 microsphere surfaces.

The FT-IR spectra (Fig. S4, Supporting information) show that the Mo–O and W–O absorption bands of $\text{Bi}_2\text{MO}_6/\text{CP}$ nanohybrids are similar to those of pure Bi_2MO_6 , which also indicates that the structures of Bi_2MO_6 were stable during the calcination process. For CP, the strong absorption bands at ~ 1710 and $\sim 1596\text{ cm}^{-1}$ are attributed to C=O and conjugated C=C stretching vibrations [25], respectively, but they cannot be observed in the spectra of the hybrids due to the low CP contents in the hybrids. The OH absorption peak at $\sim 3400\text{ cm}^{-1}$ is weak, indicating that most of the OH groups in the PVA were removed. The solid-state ^{13}C NMR spectrum of CP (Fig. S5, Supporting information) indicates the existence of conjugated polyenes, ketone [42], acetyl, and hydroxyl groups.

Fig. 3a shows the XPS survey spectra of Bi_2MO_6 , MP-2, WP-2, and CP. Peaks of Bi, Mo, O, and C appear in the XPS spectrum of MP-2, and those of Bi, W, O, and C appear in the spectrum of WP-2, which is consistent with the EDS results. The C in the survey spectra of pure Bi_2MO_6 stems from adventitious carbon [29]. In the high-resolution (HR) XPS spectra of Bi 4f for Bi_2MoO_6 and MP-2 (Fig. 3b), peaks at binding energies (E_b) of 164.3 and 159.0 eV for Bi_2MoO_6 are ascribed to $\text{Bi } 4f_{5/2}$ and $\text{Bi } 4f_{7/2}$ of $[\text{Bi}_2\text{O}_2]^{2+}$ [29], respectively. The two asymmetric peaks around E_b values of 164.3 and 159.0 eV for MP-2 can be deconvoluted into four peaks: the two peaks at 164.3 and 159.0 eV correspond to $\text{Bi } 4f_{5/2}$ and $\text{Bi } 4f_{7/2}$ of $[\text{Bi}_2\text{O}_2]^{2+}$ (as shown by the dashed lines), and the other two peaks

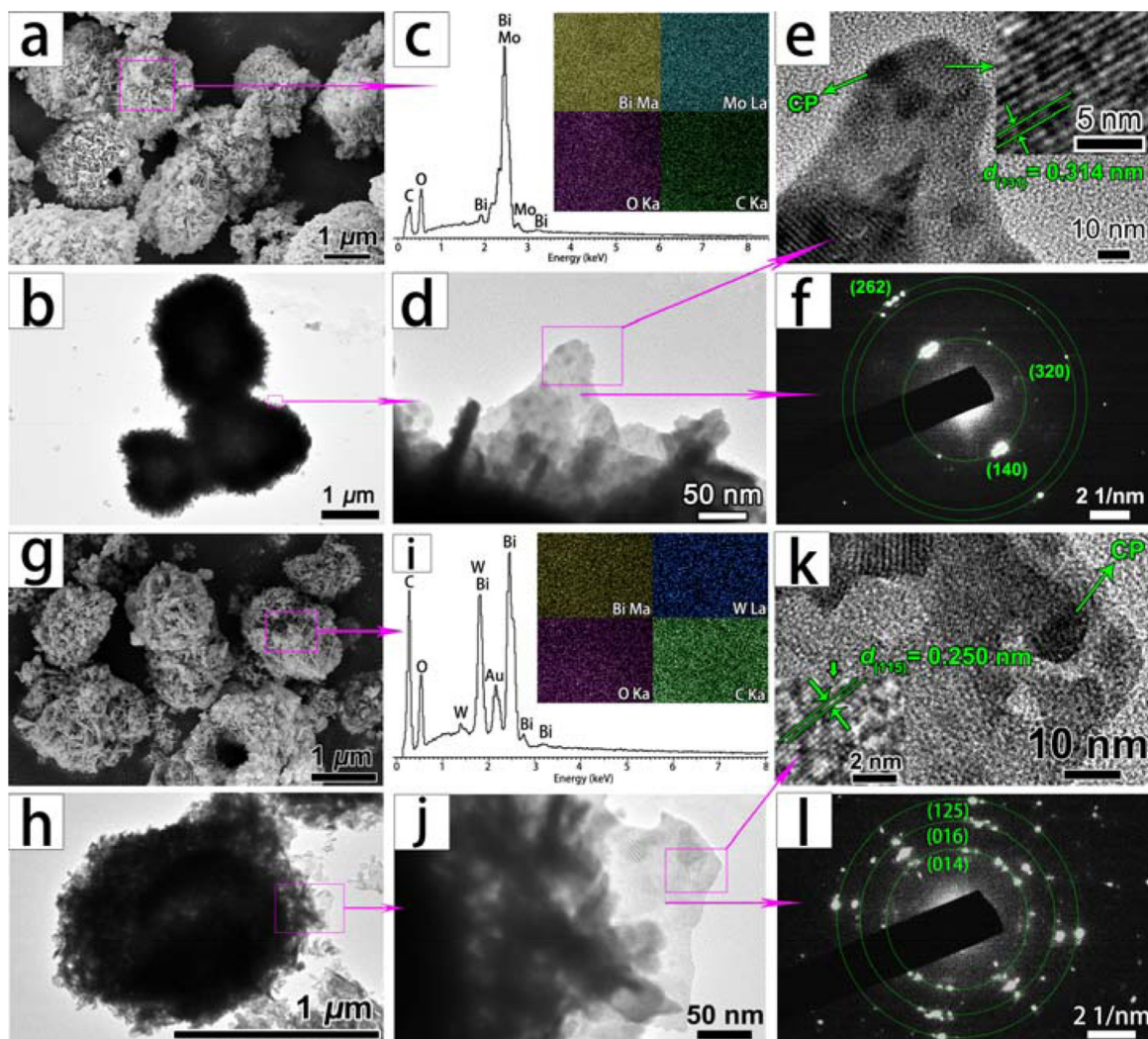


Fig. 2. SEM (a, g), EDS (c, i), TEM (b, h), HRTEM (d, e, j, k) and SAED (f, l) images of MP-2 (a–f) and WP-2 (g–l).

at 165.4 and 160.1 eV are considered to be related to the formation of Bi–O–C bonds between Bi_2MoO_6 and CP. The formation of metal –O–C bonds has been reported in the literature [25,43–45]. A similar result was obtained for WP-2, as shown in Fig. 3c. The two asymmetric peaks around E_b values of 164.5 and 159.2 eV for WP-2 can also be deconvoluted into four peaks: the two peaks at 164.5 and 159.2 eV are attributed to $[\text{Bi}_2\text{O}_2]^{2+}$ [46] (as shown by the dashed lines), and the other two peaks at 165.3 and 159.9 eV arise from the Bi^{3+} in the Bi–O–C bonds between Bi_2WO_6 and CP.

Fig. 3d shows the Mo 3d HR-XPS spectra of Bi_2MoO_6 and MP-2. For Bi_2MoO_6 , peaks at E_b values of 235.4 and 232.3 eV are attributed to Mo 3d_{3/2} and Mo 3d_{5/2} of MoO_4^{2-} [29], respectively. For MP-2, two asymmetric peaks around E_b values of 235.4 and 232.3 eV are deconvoluted into four peaks: the two peaks at 235.4 and 232.3 eV correspond to the MoO_4^{2-} (as shown by the dashed lines), and the other two peaks at 236.7 and 233.5 eV are ascribed to the Mo^{6+} in the Mo–O–C bonds that formed between Bi_2MoO_6 and CP. The W 4f HR-XPS spectra of Bi_2WO_6 and WP-2 are shown in Fig. 3e. The two peaks at E_b values of 37.6 and 35.5 eV for Bi_2WO_6 correspond to W 4f_{5/2} and W 4f_{7/2} of WO_4^{2-} [46], respectively. The asymmetric peaks around E_b values of 37.6 and 35.5 eV for WP-2 are also deconvoluted into four peaks: the two peaks at 37.6 and 35.5 eV arise from the WO_4^{2-} (as shown by the dashed lines), and the other two peaks at 38.5 and 36.3 eV are attributed to the W^{6+} in the W–O–C bonds [43] that formed between Bi_2WO_6 and CP.

Fig. 3f shows the C 1s HR-XPS spectra of MP-2, WP-2 and CP. For CP, the broad peak around E_b of 284.8 eV can be deconvoluted into four peaks. Considering the ^{13}C NMR result (Fig. S5), the peaks at 288.4, 285.9, 284.9, and 284.6 eV correspond to the C=O, C–O–H(C), C=C, and C–C bonds [47], respectively. For MP-2 and WP-2, the broad peaks around 284.7 and 284.8 eV are deconvoluted into five peaks, respectively. The four peaks at 288.4, 285.9, 284.9, and 284.6 eV correspond well with the peaks of CP, as shown by the dashed lines. The new peak at 286.5 eV is ascribed to the M–O–C bonds formed between Bi_2MoO_6 and CP. All these results indicate that metal–O–C bonds are formed at the interfaces between Bi_2MoO_6 and CP. The formation of these bonds benefits from the coordination interactions between the OH in PVA and the metal atoms in Bi_2MoO_6 .

3.2. Photocatalytic activity of $\text{Bi}_2\text{MoO}_6/\text{CP}$ nanohybrids

Adsorption equilibrium is reached for all the tested photocatalysts, after stirring for 1 h in the dark (Fig. S6, Supporting information). Under the visible light irradiation, the color of the solutions gradually becomes faded (Fig. S7, Supporting information) and the absorbance of RhB in the visible light region significantly decreases (Fig. S8, Supporting information). No corresponding increase in photoabsorption is observed in the ultraviolet region, which indicates the complete destruction of aromatic

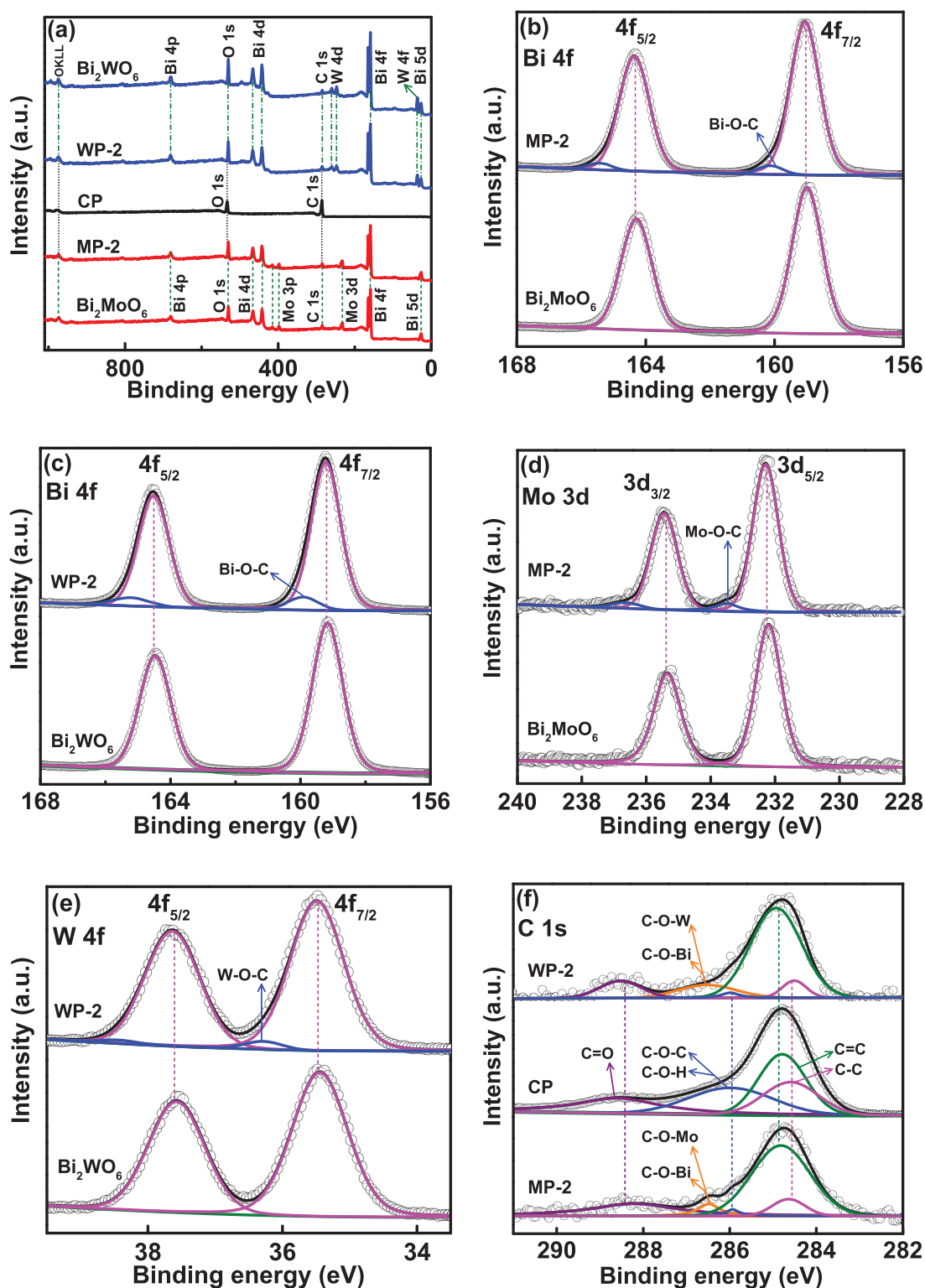


Fig. 3. XPS survey spectra (a) and high-resolution XPS spectra of Bi 4f (b, c), Mo 3d (d), W 4f (e) and C 1s (f) regions for Bi_2MoO_6 , CP, MP-2 and WP-2.

structures [29]. Fig. 4a shows that the RhB concentration hardly changes when the solution is irradiated with visible light for 160 min in the absence of any catalyst, indicating the self-photodegradation of RhB is negligible [29]. As the CP contents in the Bi_2MoO_6 /CP nanohybrids increase, the photocatalytic activity of the hybrids gradually increases, and then decreases, with MP-2 and WP-2 exhibiting the highest activities (Fig. 4a and b). The photoactivities of MP-2 and WP-2 are higher than those of commercial

N-TiO₂, the mechanical mixture of Bi_2MoO_6 and CP (MP-mix), and the mechanical mixture of Bi_2WO_6 and CP (WP-mix), as shown in Fig. 4c. The CP content in the mechanical mixtures is 1.6 wt% (S1, Supporting information). After 160 min, about 96% and 99% of RhB are removed by MP-2 and WP-2, respectively, while pure Bi_2MoO_6 and pure Bi_2WO_6 degrade <55% and <92% of the RhB, respectively.

To quantitatively investigate the reaction kinetics of RhB photodegradation by the as-prepared catalysts, the experimental data

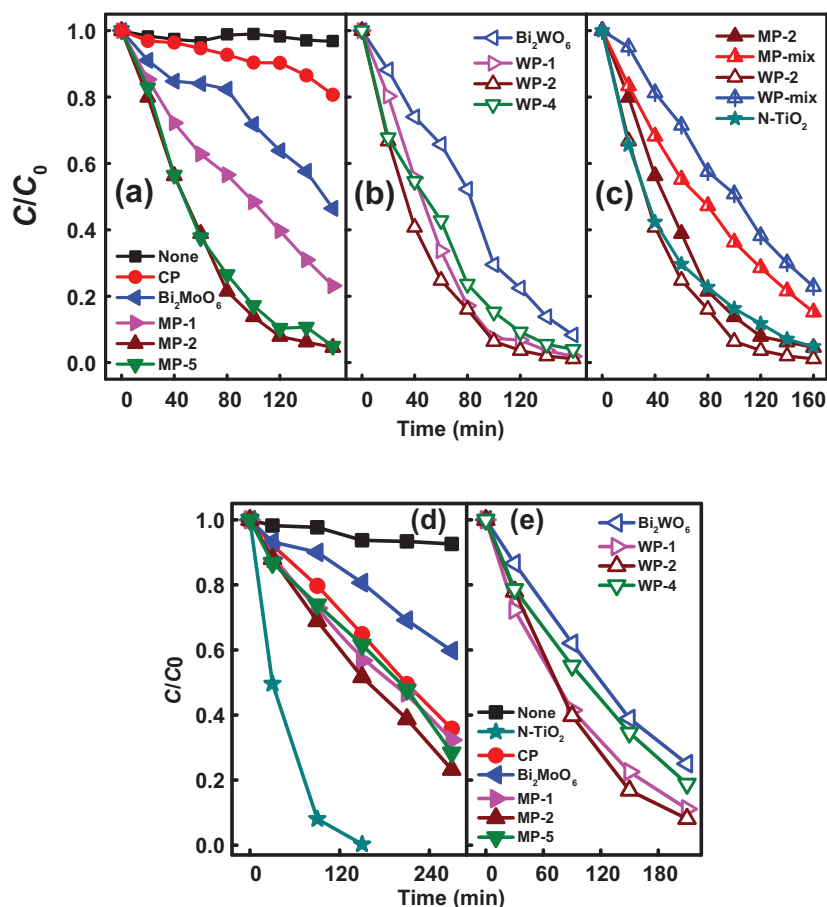


Fig. 4. Photocatalytic degradation of RhB on various catalysts under visible (a–c) and ultraviolet (d, e) light irradiation.

were fitted to a pseudo-first-order model, $-\ln(C/C_0) = kt$, where k is the apparent first-order rate constant and t is the degradation time. All curves of $\ln(C/C_0)$ vs. t exhibit linear trends (Fig. S9, Supporting information), indicating that the RhB photodegradation process is satisfactorily described by the pseudo-first-order equation. The k values for all the samples are shown in Fig. 5a. With increasing CP contents, the k values first increase and then decrease, with MP-2 and WP-2 exhibiting the maximum values of k , respectively. Our data demonstrate that the k value for MP-2 is more than four times that for Bi_2MoO_6 and about twenty times that for CP, and the k value for WP-2 is more than two times that for Bi_2WO_6 and about twenty-seven times that for CP (Fig. 5a).

In the visible light region, dye sensitization may affect the photocatalytic efficiency of photocatalysts because the RhB exhibits a strong photoabsorption (Fig. S8). To rule out the influence of dye sensitization, the photocatalytic degradation of RhB on the photocatalysts was performed under ultraviolet light irradiation [48] where the RhB exhibits a quite weak photoabsorption (Fig. S8). As shown in Figs. 4d, e and 5b, MP-2 and WP-2 exhibit higher photocatalytic efficiencies than pure Bi_2MoO_6 and CP under ultraviolet light irradiation. These results are consistent with those obtained under visible light irradiation. Under ultraviolet light irradiation, the k values for MP-2 and WP-2 are about 2.8 and 1.8 times those for Bi_2MoO_6 and Bi_2WO_6 , and about 1.4 and 3.4 times those for CP, respectively. The photoactivity enhancement of $\text{Bi}_2\text{MoO}_6/\text{CP}$ nanohybrids is reduced, compared with the data under visible light irradiation (Fig. 5a). This indicates that the dye sensitization indeed plays a role in the RhB degradation process under visible light irradiation. However, there is no doubt that the hybridization of CP and Bi_2MoO_6 can essentially enhance the pho-

tocatalytic efficiency of Bi_2MoO_6 in RhB degradation. Notably, the $\text{Bi}_2\text{MoO}_6/\text{CP}$ nanohybrids exhibit lower photocatalytic efficiencies than N-TiO_2 under ultraviolet light irradiation, which probably arises from the strong ultraviolet light absorption of N-TiO_2 [12,13].

To further reveal the CP induced photoactivity enhancements of Bi_2MoO_6 , the photocatalytic degradation of another dye methyl violet 2B on these photocatalysts were also investigated. Similar results to the RhB degradation are obtained (Fig. S10).

To better reveal the capability of CP in enhancing the photocatalytic activity of Bi_2MoO_6 , some reported photocatalytic data for graphene-containing Bi_2MoO_6 composites are compared with our results. For example, Fu et al. [49] prepared a series of hierarchical reduced graphene oxide/ Bi_2MoO_6 composites. The composites could degrade 99% of the RhB while the pure Bi_2MoO_6 degraded ~35% under visible light irradiation. Our data reveal that the MP-2 sample can degrade ~93% of RhB while Bi_2MoO_6 degrades ~35% (Fig. 4a). Sun et al. [31] reported that Bi_2WO_6 quantum dots attached onto reduced graphene oxide could degrade ~96% of RhB which was ~19% higher than the amount degraded by Bi_2WO_6 quantum dots under simulated sunlight. Our data reveal that the WP-2 sample can degrade ~96% of RhB which is also ~19% higher than the amount degraded by Bi_2WO_6 (Fig. 4b). These data indicate that the CP produced in this study was comparable with the reported CCMs (e.g., graphene) in enhancing the photocatalytic performance of semiconductors.

The stability of the photocatalysts is important for their practical application. Fig. 6 shows that, after four consecutive runs, the RhB degradation efficiencies of MP-2 and WP-2 declined by <1% and ~9%, respectively. The XRD patterns of MP-2 and WP-2 after

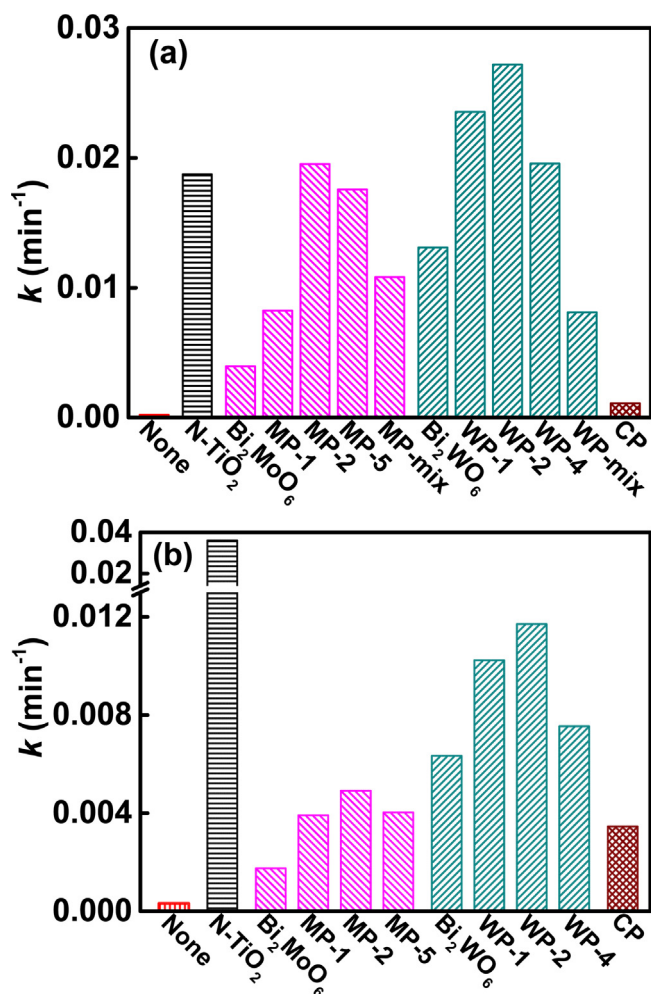


Fig. 5. Apparent first-order rate constants (k) for various photocatalysts under visible (a) and ultraviolet (b) light irradiation.

photocatalytic reactions indicate that their crystal structures remain constant (Fig. S11, Supporting information). Thus, the Bi₂MoO₆/CP nanohybrids exhibit good stability in the visible light photochemical degradation reactions.

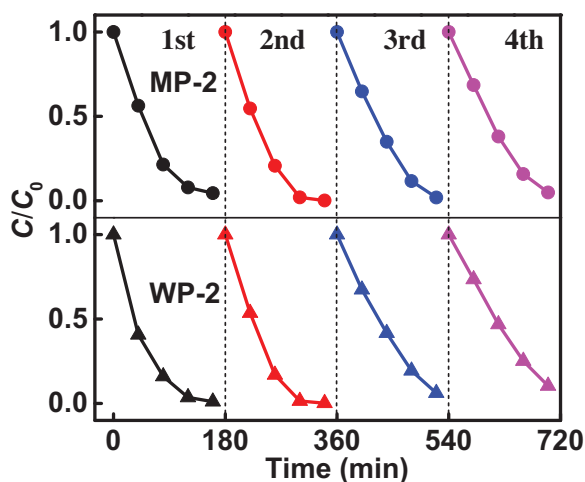


Fig. 6. Cycling runs for photocatalytic degradation of RhB on MP-2 and WP-2 under visible light irradiation.

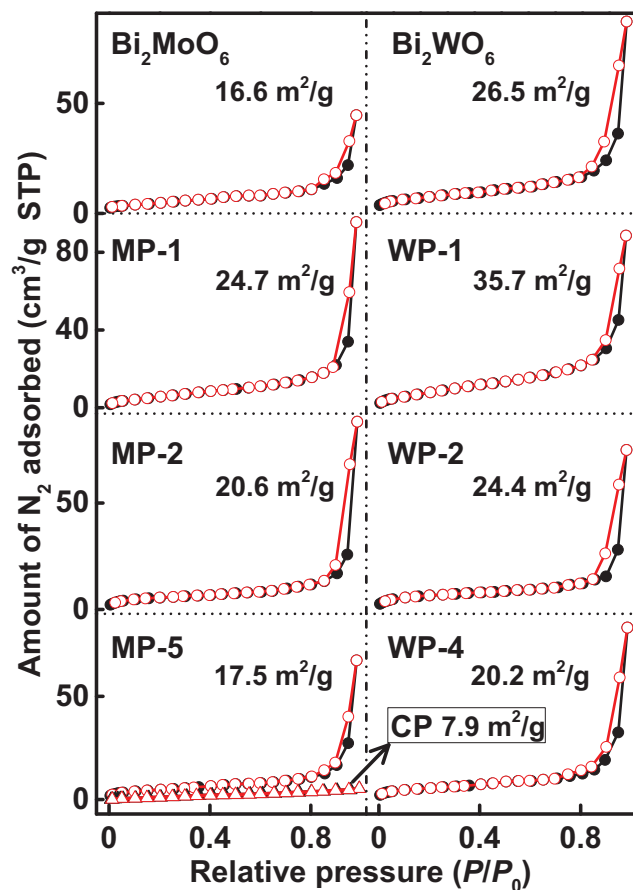


Fig. 7. N₂ adsorption-desorption isotherms of Bi₂MoO₆, CP, and their nanohybrids. The digits in the figure present the Brunauer-Emmett-Teller specific surface areas calculated from the absorption branch.

3.3. Photocatalytic mechanism

A larger specific surface area of photocatalysts can provide more surface active sites, and make charge carrier transport easier, which is favorable for the enhancement of photocatalytic performance [50]. Fig. 7 shows the N₂ adsorption-desorption isotherms of Bi₂MoO₆, CP, and their nanohybrids. All the isotherms for the Bi₂MoO₆/CP nanohybrids are of type IV, which is typically associated with capillary condensation in mesopores [51]. The isotherms show type H3 hysteresis loops at high P/P_0 , reflecting the formation of slit-shaped pores [52] by aggregation of the Bi₂MoO₆ nanosheets. The CP exhibits no hysteresis loop in its isotherm, indicating that its structure is nonporous. The Brunauer-Emmett-Teller (BET) specific surface area (S_{BET}) of CP is 7.9 m²/g, which is less than those of Bi₂MoO₆ (16.6 m²/g) and Bi₂WO₆ (26.5 m²/g). The S_{BET} values of the Bi₂MoO₆/CP nanohybrids first increase and then decrease, with increasing CP content. MP-1 and WP-1 exhibit the largest S_{BET} values, 24.7 and 35.7 m²/g, respectively. Among the two series of Bi₂MoO₆/CP nanohybrids, MP-1 and WP-4 exhibit the highest adsorption of RhB (Fig. S6). Although the photocatalytic efficiencies of MP-2 and WP-2 are the highest, their S_{BET} values and RhB adsorptions are not the highest; hence, we can conclude that neither the S_{BET} nor the dye adsorption ability is the key factor that determines the photocatalytic activity of the Bi₂MoO₆/CP nanohybrids.

The photoabsorption capability of semiconductors, which significantly influences their photocatalytic activity [16,25], was usually determined by UV-vis diffusive reflectance spectrometry. Fig. 8 shows the UV-vis diffusive reflectance spectra of Bi₂MoO₆, CP, and their nanohybrids. All the samples exhibit

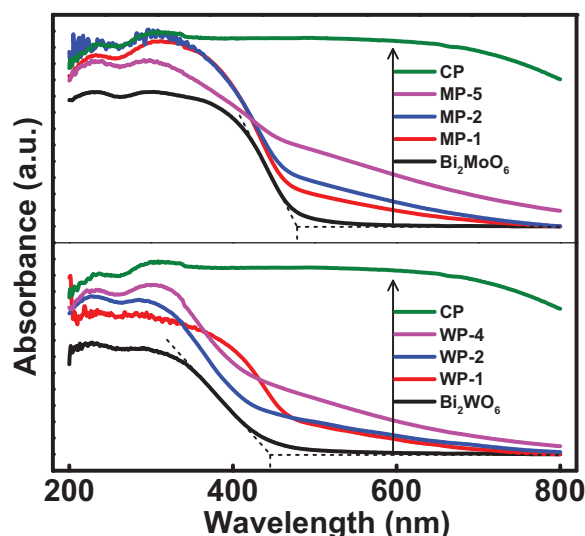


Fig. 8. UV-vis diffusive reflection spectra of Bi_2MoO_6 , CP, and their nanohybrids.

photoabsorption capability in the UV to visible regions. The absorption edges of Bi_2MoO_6 and Bi_2WO_6 are ~ 478 and ~ 446 nm (as shown by the dashed construction lines in Fig. 8), corresponding to band gaps (E_g) of 2.59 and 2.78 eV, respectively. The higher the CP content is, the stronger absorption the hybrids exhibit in visible light regions (≥ 460 nm), and the darker the color of the samples (Fig. S12, Supporting information). This is ascribed to the $\pi-\pi^*$ transition of the conjugated carbon-carbon chains in the CP layer [25]. The wide absorption band of CP in the visible light region indicates the coexistence of conjugated chains with long and short effective conjugation lengths [53], which is beneficial in increasing the light capture [25]. The photocatalytic activity enhancements of the $\text{Bi}_2\text{MoO}_6/\text{CP}$ nanohybrids, compared with the pure Bi_2MoO_6 , possibly arise from the increase in the visible light absorption capability.

To evaluate the separation efficiency of photogenerated electrons and holes, PL spectra of the samples were measured (Fig. 9). PL spectra are useful for revealing the transfer and separation efficiency of photogenerated electrons and holes. A higher PL intensity indicates a higher recombination efficiency of electrons and holes [29,54]. As shown in Fig. 9, the PL intensity of $\text{Bi}_2\text{MoO}_6/\text{CP}$ nanohybrids significantly decreases, compared with that of Bi_2MoO_6 , although the CP content is quite low ($<3\%$). The decrease of PL inten-

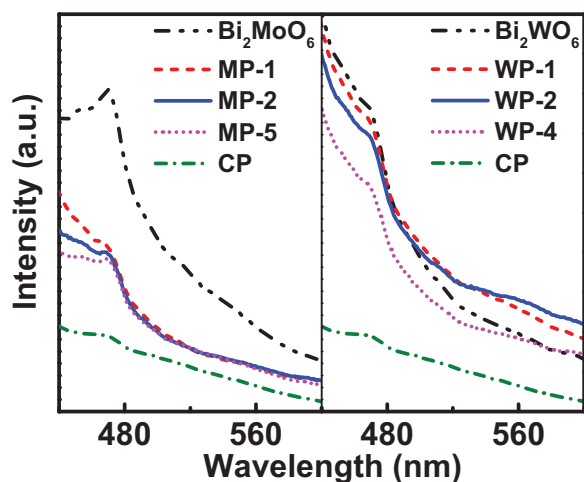


Fig. 9. PL spectra of Bi_2MoO_6 , CP, and their nanohybrids with the excitation wavelength of 400 nm.

sity for $\text{Bi}_2\text{MoO}_6/\text{CP}$ nanohybrids means that the CP decreases the recombination efficiency of the photogenerated charge carriers in Bi_2MoO_6 . The $\text{Bi}_2\text{WO}_6/\text{CP}$ nanohybrids exhibit little change in PL intensity in comparison with pure Bi_2WO_6 , indicating that CP has little effect on the recombination efficiency of the charge carriers in Bi_2WO_6 .

Time-resolved fluorescence spectroscopy was used to investigate the recombination kinetics of photoinduced charge carriers. The fluorescence intensity at 460 nm was monitored upon excitation at 370 nm. The decay spectra of Bi_2MoO_6 , CP, MP-2, and WP-2 all exhibit a multi-exponential decay process (Fig. S13, Supporting information). These spectra are all well fitted by a triple-exponential decay model (Fig. S13), with χ^2 values of 1.2–1.5 (Table 1). Their lifetimes and relative intensities are also listed in Table 1. To clearly compare the length of lifetimes of samples, their average lifetimes are calculated [55] (Table 1). The average lifetimes of Bi_2MoO_6 , MP-2, CP, WP-2, and Bi_2WO_6 are 2.863, 13.066, 3.200, 1.736, and 3.201 ns, respectively. The average lifetime of MP-2 is significantly longer than those of Bi_2MoO_6 and CP, while the average lifetime of WP-2 is shorter than those of Bi_2WO_6 and CP. This reveals that the recombination efficiency of photogenerated charge carriers in MP-2 is much lower than that in Bi_2MoO_6 and in CP, while that in WP-2 is higher than that in Bi_2WO_6 and in CP.

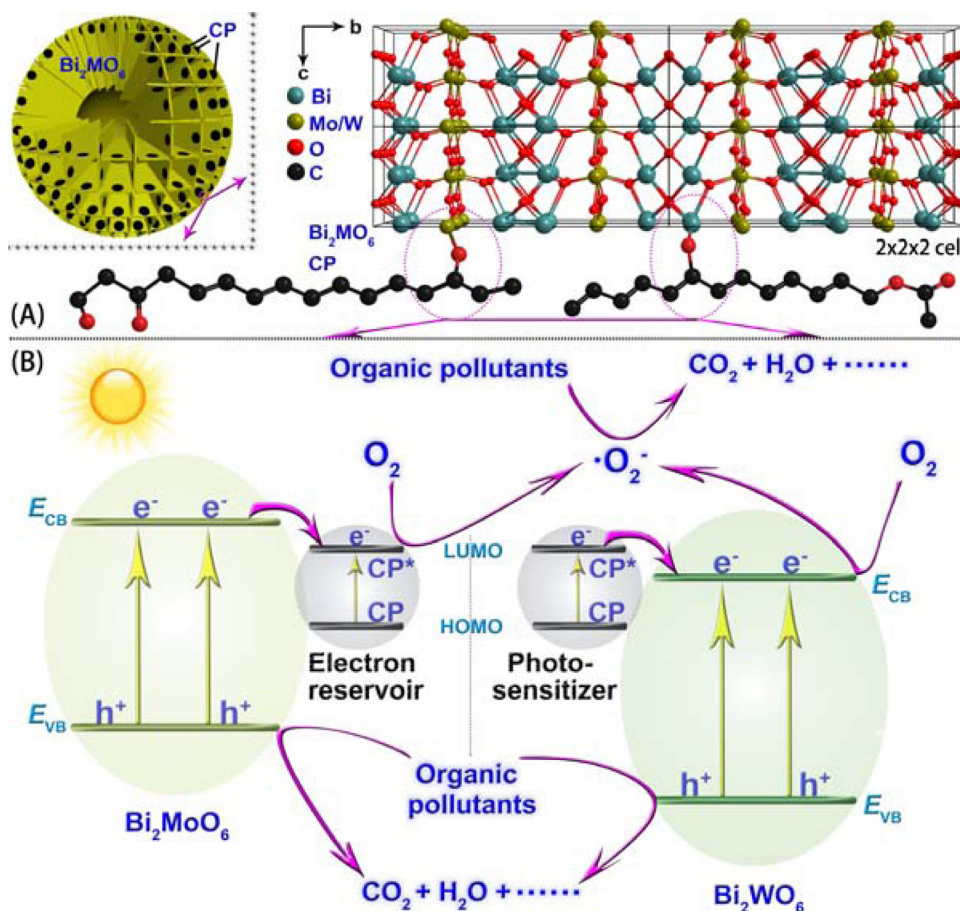
According to these results, the photocatalytic activity enhancement of $\text{Bi}_2\text{MoO}_6/\text{CP}$ nanohybrids (Figs. 4 and 5) predominantly arises from the increasing separation efficiency of photogenerated charge carriers, while that of $\text{Bi}_2\text{WO}_6/\text{CP}$ nanohybrids is ascribed to the increasing visible light absorption. Thus, CP acts as an electron reservoir [23] in the $\text{Bi}_2\text{MoO}_6/\text{CP}$ nanohybrids, while it acts as a photosensitizer [23] in the $\text{Bi}_2\text{WO}_6/\text{CP}$ nanohybrids. The enhancement of photocatalytic performance for the two series of nanohybrids relies on the electron transfer through the interface between Bi_2MoO_6 and CP [19,23]. The electron transfer processes which have been identified are shown in Scheme 1. The formation of metal $-\text{O}-\text{C}$ bonds at the interface (Scheme 1A) significantly improves the electron transfer efficiency. For the $\text{Bi}_2\text{MoO}_6/\text{CP}$ nanohybrids, the electrons in Bi_2MoO_6 are excited to the CB under visible light irradiation, and subsequently transfer to the CP at a lower energy level. A similar process occurred for the $\text{Bi}_2\text{MoO}_6/\text{graphene}$ hybrids [30]. The CP itself can also be excited to provide electrons, and the slight photodegradation of RhB on CP (Figs. 4 and 5) clarifies this. The electrons can react with the adsorbed oxygen to form the superoxide radical ($\cdot\text{O}_2^-$) [29,30] which is an efficient oxidant. Holes are left in the valence band (VB) of Bi_2MoO_6 , and they can transfer to the surface of the catalysts to oxidize the organic pollutants. This transfer process of electrons increases the separation efficiency of photogenerated electrons and holes, which greatly favors the improvement of photocatalytic performance. In this case, CP behaves as an electron reservoir to accept and shuttle the electrons [19,30,54,56]. For the $\text{Bi}_2\text{WO}_6/\text{CP}$ nanohybrids, both Bi_2WO_6 and CP are capable of absorbing the visible light. The photogenerated electrons transfer from the CP, which has a

Table 1

Lifetimes (τ_1 , τ_2 , τ_3 and τ_m) and relative intensities (int) obtained by fitting the time-resolved fluorescence decay spectra (Fig. S13, Supporting information) of Bi_2MoO_6 , CP, MP-2, and WP-2 to a triple-exponential decay model.

Sample	τ_1/ns (int ₁)	τ_2/ns (int ₂)	τ_3/ns (int ₃)	τ_m^a/ns	χ^2
Bi_2MoO_6	0.761 (0.793)	1.881 (0.152)	6.953 (0.054)	2.863	1.384
MP-2	0.938 (0.861)	2.716 (0.103)	26.414 (0.036)	13.066	1.472
CP	0.884 (0.841)	3.014 (0.097)	7.169 (0.062)	3.200	1.282
WP-2	0.242 (0.607)	0.998 (0.346)	4.148 (0.047)	1.736	1.372
Bi_2WO_6	0.924 (0.897)	2.816 (0.089)	13.528 (0.014)	3.201	1.394

$$^a \text{Average lifetime, } \tau_m = \frac{\sum_{i=1}^3 (\tau_i^2 \cdot \text{int}_i)}{\sum_{i=1}^3 (\tau_i \cdot \text{int}_i)}.$$



Scheme 1. Schematic illustration for interface structures between Bi_2MoO_6 and CP (A), and processes of separation and transfer of photogenerated charge carriers in $\text{Bi}_2\text{MoO}_6/\text{CP}$ nanohybrids (B).

narrow band gap, to the CB of Bi_2WO_6 , which has a wide band gap, since the energy level of the CP is higher than the CB level of Bi_2WO_6 , just like the dye sensitization process [57]. The electrons then reduce the adsorbed oxygen to give $\cdot\text{O}_2^-$ [58–62]. In this case, CP behaves as a photosensitizer [19,23,24]. It broadens the photoabsorption range of Bi_2WO_6 but shows no contribution to the separation efficiency of the photogenerated charge carriers in Bi_2WO_6 . The CP content of the $\text{Bi}_2\text{MoO}_6/\text{CP}$ nanohybrids should be optimized because too much CP would cover the active sites on the surfaces of Bi_2MoO_6 microspheres [63] and decrease the photocatalytic activity of the nanohybrids (Figs. 4 and 5).

The CB and VB levels of Bi_2MoO_6 are determined according to the empirical equation $E_{\text{VB}} = \text{not a subscript } X - E_e + 0.5E_g$ [29], where X is the electronegativity of the semiconductor, which is the geometric mean of the electronegativity of its constituent atoms, and E_e is the energy of the free electrons on the hydrogen scale (about 4.5 eV). The X values for Bi_2MoO_6 and Bi_2WO_6 are 5.55 [29] and 6.36 eV [64], respectively. According to the E_g values obtained from UV–vis diffusive reflection spectra (Fig. 8), the CB and VB levels of Bi_2MoO_6 are calculated to be -0.25 and $+2.34$ eV, and those of Bi_2WO_6 are calculated to be $+0.47$ and $+3.25$ eV, respectively, consistent with the reported results in the literature [58,65,66]. Both Bi_2MoO_6 and Bi_2WO_6 are n-type semiconductors [29,67], and the former exhibits a higher CB level than the latter, which is consistent with the proposed mechanism in Scheme 1.

In the photodegradation process of RhB on the $\text{Bi}_2\text{MoO}_6/\text{CP}$ nanohybrids, holes (h^+), electrons (e^-), superoxide radicals ($\cdot\text{O}_2^-$), and hydroxyl radicals ($\cdot\text{OH}$) are all possible active species. The corresponding scavengers are used to investigate their roles (Fig. S14,

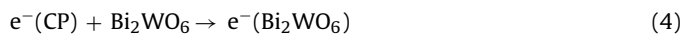
Supporting information). The results show that $\cdot\text{O}_2^-$ and h^+ are the predominant active species.

According to the above discussion, the most probable reactions occurring in the photodegradation process of RhB are:

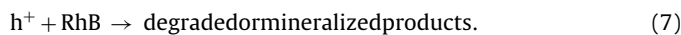
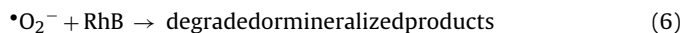
for $\text{Bi}_2\text{MoO}_6/\text{CP}$ nanohybrids



for $\text{Bi}_2\text{WO}_6/\text{CP}$ nanohybrids



and for $\text{Bi}_2\text{MoO}_6/\text{CP}$ nanohybrids



4. Conclusion

The $\text{Bi}_2\text{MoO}_6/\text{CP}$ nanohybrids were prepared successfully via calcining the precursors, $\text{Bi}_2\text{MoO}_6/\text{PVA}$ composites. SEM, TEM, and EDS mapping images indicate that the CP homogeneously distributes on the surface of the Bi_2MoO_6 hollow microspheres. XPS spectra confirm the formation of metal (Bi and Mo or W)–O–C bonds at the interfaces between Bi_2MoO_6 and CP, which form due to the coordination of hydroxyl groups in PVA to the metal atoms in Bi_2MoO_6 . The $\text{Bi}_2\text{MoO}_6/\text{CP}$ nanohybrids exhibit higher photocatalytic

efficiencies for degrading RhB under visible and ultraviolet light irradiation than pure Bi_2MoO_6 . Interestingly, two different mechanisms by which CP enhances the photocatalytic activity of Bi_2MoO_6 were confirmed. For the $\text{Bi}_2\text{MoO}_6/\text{CP}$ nanohybrids, the CP acts as an electron reservoir, accepting and shuttling the electrons from Bi_2MoO_6 . For the $\text{Bi}_2\text{WO}_6/\text{CP}$ nanohybrids, however, the CP acts as a photosensitizer, injecting electrons into Bi_2WO_6 . The metal (Bi and Mo or W) —O—C bonds formed at the interfaces substantially promote the electron transfer. These nanohybrid photocatalysts exhibit good stability and recyclability. The $\bullet\text{O}_2^-$ and h^+ play significant roles in the RhB photodegradation process. This work indicates that CP may be used as a substitute for graphene, fullerenes, and CNTs in modifying semiconductors to enhance their photocatalytic performance, in view of its lower cost and easier preparation. To further verify these results, several CP-containing nanohybrid photocatalysts should be synthesized and evaluated in the future.

Acknowledgements

The present work is supported financially by the National Natural Science Foundation of China (no. 21173135) and the Specialized Research Fund for the Doctoral Program of Higher Education of China (no. 20110131130008).

Appendix A. Supplementary data

Supplementary data associated with this article can be found, in the online version, at <http://dx.doi.org/10.1016/j.apcatb.2015.02.005>.

References

- [1] X. Chen, S. Shen, L. Guo, S.S. Mao, *Chem. Rev.* 110 (2010) 6503–6570.
- [2] M. Aresta, A. Dibenedetto, A. Angelini, *Chem. Rev.* 114 (2014) 1709–1742.
- [3] L. Jing, W. Zhou, G. Tian, H. Fu, *Chem. Soc. Rev.* 42 (2013) 9509–9549.
- [4] W.-J. Ong, L.-L. Tan, S.-P. Chai, S.-T. Yong, A.R. Mohamed, *ChemSusChem* 7 (2014) 690–719.
- [5] X. Wang, M. Liao, Y. Zhong, J.Y. Zheng, W. Tian, T. Zhai, C. Zhi, Y. Ma, J. Yao, Y. Bando, D. Golberg, *Adv. Mater.* 24 (2012) 3421–3425.
- [6] J. Tian, Y. Sang, G. Yu, H. Jiang, X. Mu, H. Liu, *Adv. Mater.* 25 (2013) 5075–5080.
- [7] C. Yu, G. Li, S. Kumar, K. Yang, R. Jin, *Adv. Mater.* 26 (2014) 892–898.
- [8] Q. Hua, T. Cao, H. Bao, Z. Jiang, W. Huang, *ChemSusChem* 6 (2013) 1966–1972.
- [9] F.X. Xiao, J. Miao, B. Liu, *J. Am. Chem. Soc.* 136 (2014) 1559–1569.
- [10] Y. Zheng, J. Liu, J. Liang, M. Jaroniec, S.Z. Qiao, *Energy Environ. Sci.* 5 (2012) 6717–6731.
- [11] S. Cao, J. Yu, *J. Phys. Chem. Lett.* 5 (2014) 2101–2107.
- [12] A. Fujishima, X. Zhang, D.A. Tryk, *Surf. Sci. Rep.* 63 (2008) 515–582.
- [13] W.-K. Jo, J.-T. Kim, *J. Hazard. Mater.* 164 (2009) 360–366.
- [14] Y. Zhang, Z. Chen, S. Liu, Y.-J. Xu, *Appl. Catal. B* 140–141 (2013) 598–607.
- [15] J.G. Yu, Y.R. Su, B. Cheng, *Adv. Funct. Mater.* 17 (2007) 1984–1990.
- [16] R. Asahi, T. Morikawa, T. Ohwaki, K. Aoki, Y. Taga, *Science* 293 (2001) 269–271.
- [17] J.N. Wilson, H. Idriss, *J. Am. Chem. Soc.* 124 (2002) 11284–11285.
- [18] A. Hameed, T. Montini, V. Gombac, P. Fornasiero, *J. Am. Chem. Soc.* 130 (2008) 9658–9659.
- [19] C.J. Shearer, A. Cherevan, D. Eder, *Adv. Mater.* 26 (2014) 2295–2318.
- [20] D. Chen, H. Zhang, Y. Liu, J. Li, *Energy Environ. Sci.* 6 (2013) 1362–1387.
- [21] H. Tang, C.M. Hessel, J. Wang, N. Yang, R. Yu, H. Zhao, D. Wang, *Chem. Soc. Rev.* 43 (2014) 4281–4299.
- [22] M.Q. Yang, N. Zhang, Y.J. Xu, *ACS Appl. Mater. Interfaces* 5 (2013) 1156–1164.
- [23] Y. Zhang, N. Zhang, Z.-R. Tang, Y.-J. Xu, *ACS Nano* 6 (2012) 9777–9789.
- [24] K. Woan, G. Pyrgiotakis, W. Sigmund, *Adv. Mater.* 21 (2009) 2233–2239.
- [25] P. Lei, F. Wang, S. Zhang, Y. Ding, J. Zhao, M. Yang, *ACS Appl. Mater. Interfaces* 6 (2014) 2370–2376.
- [26] Y. Zhou, E. Antonova, W. Bensch, G.R. Patzke, *Nanoscale* 2 (2010) 2412–2417.
- [27] G. Tian, Y. Chen, W. Zhou, K. Pan, Y. Dong, C. Tian, H. Fu, *J. Mater. Chem.* 21 (2011) 887–892.
- [28] H. Li, Q. Deng, J. Liu, W. Hou, N. Du, R. Zhang, X. Tao, *Catal. Sci. Technol.* 4 (2014) 1028–1037.
- [29] H. Li, J. Liu, W. Hou, N. Du, R. Zhang, X. Tao, *Appl. Catal. B* 160–161 (2014) 89–97.
- [30] P. Wang, Y. Ao, C. Wang, J. Hou, J. Qian, *Carbon* 50 (2012) 5256–5264.
- [31] S. Sun, W. Wang, L. Zhang, *J. Phys. Chem. C* 117 (2013) 9113–9120.
- [32] H. Ma, J. Shen, M. Shi, X. Lu, Z. Li, Y. Long, N. Li, M. Ye, *Appl. Catal. B* 121–122 (2012) 198–205.
- [33] X. Zhao, H. Liu, Y. Shen, J. Qu, *Appl. Catal. B* 106 (2011) 63–68.
- [34] S. Zhu, T. Xu, H. Fu, J. Zhao, Y. Zhu, *Environ. Sci. Technol.* 41 (2007) 6234–6239.
- [35] M. Yang, G. Pang, L. Jiang, S. Feng, *Nanotechnology* 17 (2006) 206–212.
- [36] A. Singhal, M. Kaur, K. Dubey, Y. Bhardwaj, D. Jain, C. Pillai, A. Tyagi, *RSC Adv.* 2 (2012) 7180–7189.
- [37] J.H. Kim, B.R. Min, K.B. Lee, J. Won, Y.S. Kang, *Chem. Commun.* 38 (2002) 2732–2733.
- [38] F. Trifiro, H. Hoser, R.D. Scarle, *J. Catal.* 25 (1972) 12–24.
- [39] H. Cheng, B. Huang, Y. Liu, Z. Wang, X. Qin, X. Zhang, Y. Dai, *Chem. Commun.* 48 (2012) 9729–9731.
- [40] C. Albornoz, E.E. Sileo, S.E. Jacobo, *Physica B* 354 (2004) 149–153.
- [41] X.-F. Qian, J. Yin, J.-C. Huang, Y.-F. Yang, X.-X. Guo, Z.-K. Zhu, *Mater. Chem. Phys.* 68 (2001) 95–97.
- [42] B. Holland, J. Hay, *Polymer* 42 (2001) 6775–6783.
- [43] M.J. Zhou, N. Zhang, Z.H. Hou, *Int. J. Photoenergy* 2014 (2014) 1–6.
- [44] O. Akhavan, R. Azimirad, S. Safa, *Mater. Chem. Phys.* 130 (2011) 598–602.
- [45] B.L. Hurley, R.L. McCreery, *J. Electrochem. Soc.* 151 (2004) B252–B259.
- [46] R. Shi, G. Huang, J. Lin, Y. Zhu, *J. Phys. Chem. C* 113 (2009) 19633–19638.
- [47] S.D. Gardner, C.S. Singamsetty, G.L. Booth, G.-R. He, C.U. Pittman Jr., *Carbon* 33 (1995) 587–595.
- [48] X. Yan, T. Ohno, K. Nishijima, R. Abe, B. Ohtani, *Chem. Phys. Lett.* 429 (2006) 606–610.
- [49] G. Tian, Y. Chen, J. Zhou, C. Tian, R. Li, C. Wang, H. Fu, *CrystEngComm* 16 (2014) 842–849.
- [50] Q. Xiang, B. Cheng, J. Yu, *Appl. Catal. B* 138–139 (2013) 299–303.
- [51] S. Cho, J.-W. Jang, E.S. K.-j. Kong, Kim, K.-H. Lee, J.S. Lee, *Adv. Funct. Mater.* 23 (2013) 2348–2356.
- [52] J.L. Gunjaker, I.Y. Kim, J.M. Lee, N.S. Lee, S.J. Hwang, *Energy Environ. Sci.* 6 (2013) 1008–1017.
- [53] H.-c. Liang, X.-z. Li, *Appl. Catal. B* 86 (2009) 8–17.
- [54] X. An, K. Li, J. Tang, *ChemSusChem* 7 (2014) 1086–1093.
- [55] T. Sen, A. Patra, *J. Phys. Chem. C* 112 (2008) 3216–3222.
- [56] Q. Li, B. Guo, J. Yu, J. Ran, B. Zhang, H. Yan, J.R. Gong, *J. Am. Chem. Soc.* 133 (2011) 10878–10884.
- [57] H. Fu, C. Pan, W. Yao, Y. Zhu, *J. Phys. Chem. B* 109 (2005) 22432–22439.
- [58] Y. Tian, B. Chang, J. Lu, J. Fu, F. Xi, X. Dong, *ACS Appl. Mater. Interfaces* 5 (2013) 7079–7085.
- [59] D. He, L. Wang, D. Xu, J. Zhai, D. Wang, T. Xie, *ACS Appl. Mater. Interfaces* 3 (2011) 3167–3171.
- [60] P. Ju, P. Wang, B. Li, H. Fan, S. Ai, D. Zhang, Y. Wang, *Chem. Eng. J.* 236 (2014) 430–437.
- [61] Y. Liu, M. Zhang, L. Li, X. Zhang, *Appl. Catal. B* 160–161 (2014) 757–766.
- [62] D. Wang, L. Guo, Y. Zhen, L. Yue, G. Xue, F. Fu, *J. Mater. Chem. A* 2 (2014) 11716–11727.
- [63] J. Zhang, J. Yu, M. Jaroniec, J.R. Gong, *Nano Lett.* 12 (2012) 4584–4589.
- [64] Z. Zhang, W. Wang, L. Wang, S. Sun, *ACS Appl. Mater. Interfaces* 4 (2012) 593–597.
- [65] Y.S. Xu, W.D. Zhang, *Dalton Trans.* 42 (2013) 1094–1101.
- [66] F.-J. Zhang, S.-F. Zhu, F.-Z. Xie, J. Zhang, Z.-D. Meng, *Sep. Purif. Technol.* 113 (2013) 1–8.
- [67] Y. Peng, M. Yan, Q.-G. Chen, C.-M. Fan, H.-Y. Zhou, A.-W. Xu, *J. Mater. Chem. A* 2 (2014) 8517–8524.